

Ultra-miniaturized Bloch mode metasplitters for one-dimensional grating waveguides

Ahmet Oguz Sakin¹, Hamza Kurt², Mehmet Unlu^{1*}

¹Department of Electrical and Electronics Engineering, TOBB University of Economics and Technology, Ankara, Turkey

²School of Electrical Engineering, Korea Advanced Institute of Science and Technology (KAIST), Daejeon, Republic of Korea

*Corresponding author: munlu@etu.edu.tr

ABSTRACT

We present, for the first time, power splitters with multiple channel configurations in one-dimensional grating waveguides (1DGWs) that maintain crystal lattice-sensitive Bloch mode profiles without perturbation across all output channels, all within an ultra-miniaturized footprint of just $2.1 \times 2.2 \mu\text{m}^2$. This novel capability reduces the need for transition regions, simplifies multi-channel configurations of 1DGWs, and maximizes the effective use of chip area. The pixelated metamaterial approach, integrated with a time-domain heuristic algorithm, is utilized to concurrently achieve broadband operation, optimized dispersion control, and minimal loss. We experimentally demonstrate that our 1x2 and 1x3 metasplitters achieve average minimum losses per channel of 3.80 dB and 5.36 dB, respectively, which are just 0.80 dB and 0.59 dB above ideal splitting. The measurements for both designs demonstrate a 1 dB bandwidth of 15 nm, with excellent uniformity across all output channels. These versatile metasplitter designs can serve as fundamental building blocks for ultrahigh-bandwidth, densely integrated photonic circuits and in scenarios where slow light is essential.

Keywords Silicon photonics, Bloch mode, grating waveguides, pixelated metamaterials, inverse design

1 Introduction

1DGWs are meticulously engineered artificial structures designed to control light propagation by manipulating lattice-sensitive Bloch modes. These waveguides have emerged as promising components in cutting-edge applications, including microwave photonics [1], signal processing [2], quantum photonics [3], optical modulators [4]. In these applications, multi-channel configurations are predominantly utilized to optimize system performance, increase capacity, and enhance scalability. To achieve these goals, power splitting is a key operation in 1DGWs, which is conventionally achieved using multimode interferometers (MMIs) [5], directional couplers [6], Y-branches [7], or photonic crystals [8]. However, integrating 1DGWs with traditional power splitters presents challenges due to disparities in dispersion properties and mode profiles.

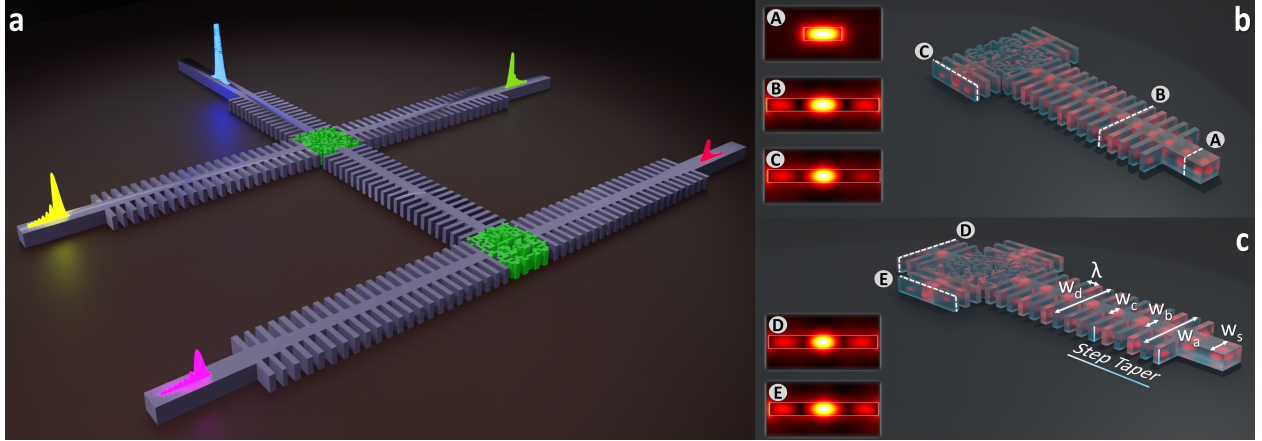


Figure 1: (a) Schematics of the 1x2 and 1x3 metasplitters designed for Bloch mode splitting in multi-channel 1DGW-based systems (Different colored outputs highlight the possibility of pulse customization between channels with varying periods). (b) Close-up of the 1x2 metasplitter with 1DGW connections, highlighting Bloch mode splitting capabilities and corresponding mode profiles (A–C). (c) Dimensions of 1DGWs and close-up of the 1x3 metasplitter with corresponding mode profiles (D–E).

Consequently, channels are initially divided using conventional power dividers before employing 1DGWs, leading to significant chip area consumption and increased system complexity.

These challenges are particularly evident in true-time delay line configurations, which demand substantial chip space. Moreover, design complexity in these systems further increases when conventional power splitters are used to expand channels or accommodate complex 2D configurations, especially in antenna array systems [9, 10, 11]. A specific problem arises since power splitting does not occur as light propagates through the 1DGW structure, it is necessary to use double-step taper structures—one on the input side and one on the output side—between the strip waveguide and 1DGW structures in each channel. This design requirement presents a significant challenge, especially in scenarios with high group index-based 1DGWs, as achieving perfect coupling ratios in the transitions is difficult [12]. By implementing power splitting in 1DGWs, the number of step taper structures in a system with L channels can be reduced from $2L$ to $L + 1$. This new configuration includes only one taper structure at the input and the remaining transitions at the outputs. However, even with the emergence of this new configuration concept, the conventional design approach remains challenging for power splitting in 1DGWs. This is due to the high group index sensitivity, strongly wavelength-selective nature, and lattice-sensitive Bloch mode profiles, which are difficult to address when relying on the designer’s intuition. Therefore, a substantial challenge persists in developing ultra-compact and low-loss Bloch mode splitters for 1DGWs.

In this Letter, we present, to the best of our knowledge, the first Bloch mode power splitters for 1DGWs, demonstrated in 1x2 and 1x3 configurations, which occupies a footprint of only $2.1 \times 2.2 \mu\text{m}^2$. The dependence of Bloch modes on the crystal lattice structure sets them apart from standard photonic design libraries. To effectively address the challenges of light manipulation within this framework, inverse design methods have been rigorously explored [13]. Among these, we prefer the pixelated metamaterial approach,

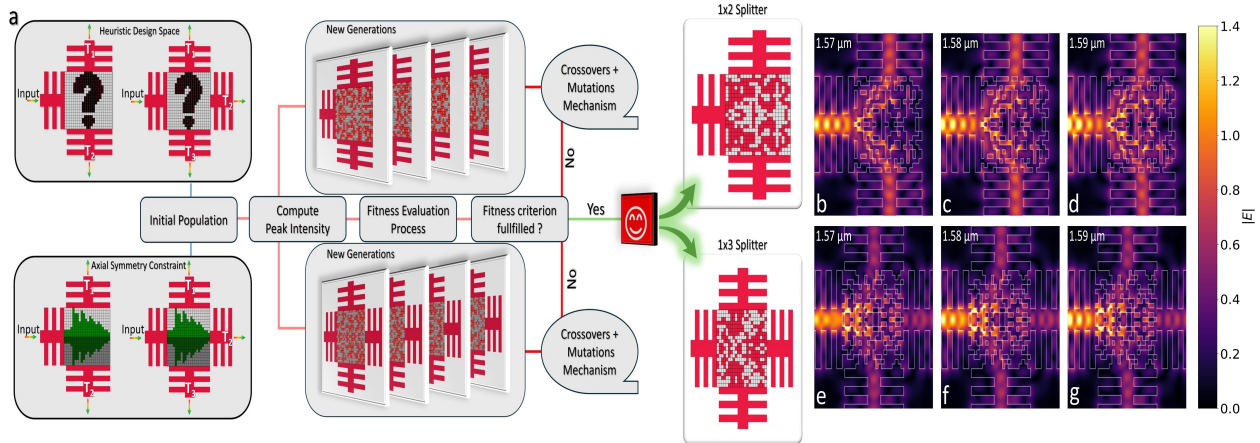


Figure 2: (a) Flowchart of the heuristic algorithm used for the inverse design of 1x2 and 1x3 metasplitters. (b–d) E-field distributions of the 1x2 metasplitter at 1.57 μm , 1.58 μm , 1.59 μm . (e–g) E-field distributions of the 1x3 metasplitter at the same wavelengths.

which balances design complexity and simplicity [14]. This method optimizes key interdependent parameters, including broadband performance, uniformity, and dispersive compatibility using heuristic algorithms.

Figure 1-(a) depicts a multi-channel 1DGW system that includes both 1x2 and 1x3 pixelated metasplitters. In 1DGWs, light propagates as Bloch mode profiles, consistent with the crystal lattice of the structure, due to the interaction between the light wave and the periodic grating structures. Therefore, the design of ultra-miniaturized metasplitters must ensure the preservation of a consistent Bloch mode profile. Typically, the Bloch field intensity reaches the tips of the grating; thus, designing metasplitters smaller than the grating width could potentially disrupt this Bloch mode profile. In Figure 1-(b), the mode labeled A corresponds to the TE fundamental mode, which, after the transition region, evolves into the mode labeled B, representing the Bloch mode profile, reaching the tip of the grating structures as depicted. As illustrated in Figure 1-(c), the inner waveguide width of the 1DGW is denoted as w_c , the width of the corrugated section as w_d , and the period as Λ . Group-velocity mismatch occurs in the butt coupling from the strip waveguide, which has a width w_s , to the grating waveguide. To minimize band narrowing and decreases in the coupling ratio, a step taper structure based on the anti-Fresnel reflection method is employed [12, 15]. The step taper design gradually narrows from w_s to w_c , as shown in Figure 1-(c), with five distinct widths, denoted as w_b . In the toothed segment design, the parameter w_a is uniformly selected to be less than 100 nm, as compared to the corrugated part of the grating waveguide (w_d). The 1DGW topology has been optimized to achieve a broadband true-time delay in the L-band, with a group index of 6.2 at 1580 nm (Sect. S1, Supplement I). Therefore, the grating period (Λ), corrugation width (w_d), and inner waveguide width (w_c) are set to 380 nm, 2100 nm, and 450 nm, respectively. The device is designed on a silicon-on-insulator (SOI) wafer, consisting of a 220 nm thick silicon device layer and a 2 μm thick buried oxide (BOX) layer. The strip waveguide width (w_s) is set to 700 nm to support two TE-like modes and two TM-like modes.

The metasplitter design area is specified as 2.1 $\mu\text{m} \times 2.2 \mu\text{m}$, ensuring that both dimensions exceed the grating width, as previously mentioned. This specification provides the most feasible boundaries for a highly

miniaturized design region. Considering the computational cost of inverse design and specific fabrication constraints, the square pixel size is set to $100 \text{ nm} \times 100 \text{ nm}$. This design method indicates that the material properties are binary, consisting of either silicon or silicon dioxide. As shown in Figure 2-(a), the inverse design flowchart for the metasplitters, utilizing the genetic algorithm, is illustrated.

The process starts with an initial random population of designs within a heuristic design space, defined by specific dimensions. To ensure consistent performance across different channels and simultaneously reduce computational cost, an axial symmetry constraint is applied. The most challenging aspect of this work is maintaining low insertion loss while ensuring high uniformity across a broad bandwidth. Therefore, selecting an appropriate Figure of Merit (FoM) is crucial. It is well established that a temporal signal can be designed to encompass all relevant frequencies of interest. Therefore, utilizing temporal signals facilitates the efficient design of metastructures with the desired dispersion characteristics and uniformity across a broadband spectrum. In line with this approach, and considering the spectral characteristics of 1DGWs, an ultra-short signal with a duration of 90 fs at 1580 nm is employed as the input. Evaluating the output signals can determine whether the designed metasplitters have the proper group-velocity profile, uniformity, and broadband characteristics. Problems in these areas often result in temporal broadening and distortion of the ultra-short pulse shape, leading to reduced peak intensity [16] (Sect. S2, Supplement I). Therefore, the suitable FoM of a $1 \times N$ power splitter system can be formulated as shown in Equation 1.

$$\text{FoM} = \alpha \left[1 - 2 \left(\sum_{i=1}^{N_s} S_p^i(t) \right) - S_p^{N_s+1}(t) \cdot \xi \right] + \beta \sum_{i=1}^{N_s+\xi} \sum_{j=i+1}^{N_s+\xi} |S_p^i(t) - S_p^j(t)| \quad (1)$$

Here, $S_p^i(t)$ and $S_p^j(t)$ represent the peak values of the time-domain Poynting vector for channels. α and β are weighting factors. N_s represents the number of symmetric channels, where $N_s = \frac{N}{2}$ for even N and $N_s = \frac{N-1}{2}$ for odd N . Additionally, $\xi = 1$ if N is odd and $\xi = 0$ if N is even. The first term of the FoM ensures overall efficiency, while the second term promotes uniformity among channels. Due to symmetry, only half of the channels are considered for the sums and uniformity. As a result, the FoM for the 1×2 splitter is defined as $\text{FoM} = 1 - 2(S_p^1(t))$, while for the 1×3 splitter it is defined as $\text{FoM} = \alpha[1 - 2S_p^1(t) - S_p^2(t)] + \beta|S_p^1(t) - S_p^2(t)|$. Each design is evaluated using a fitness check. If it doesn't meet the criteria, new designs are generated through crossovers and mutations.

To assess the designs, we use 3D Finite-Difference Time-Domain (FDTD) simulations, as 2D simulations, though computationally efficient, fall short of accurately capturing losses and mode profiles, especially for the Bloch mode in 1DGWs [17]. The simulated E-field results show effective light division into two and three channels for both metasplitters, as illustrated in Figure 2-(b) to (g). In Figure 2-(b) to (d), the 1×2 metasplitter separates high and low field intensities of the Bloch mode without mode conversion, as supported by the simulated E-field profile shown in Figure 1-(b), labeled C. For the 1×3 metasplitter, the

Bloch mode distributes power into three channels, as shown in Figure 2-(e) to (g), with the Bloch mode profile preserved in the simulated E-field models D and E in Figure 1-(c).

The metasplitters are fabricated using electron beam lithography, as part of the NanoSOI multi-project wafer process by Applied Nanotools (ANT) [18]. The scanning electron microscope (SEM) images of the meta devices are shown in Figure 3-(a) and (b). To characterize the metasplitters, the input signal is coupled into a grating coupler using a polarization-maintaining fiber (PMF), while the output signal for each channel is guided through a PMF with a grating coupler and subsequently measured with Agilent 81635A optical power sensors, which operate within a bandwidth of 1480-1580 nm. To eliminate the influence of grating couplers on the characterization results, a grating coupler-straight waveguide-grating coupler structure is employed.

Figure 3-(c) presents the simulation result of the 1DGW, which shows a 1 dB bandwidth of 39 nm and a loss of 0.74 dB at 1580 nm. As shown in Figure 3-(d) and (e), the simulated transmission spectra are presented for both the conventional strip waveguide (WG) and the metasplitter-based configurations used for power splitting. In Figure 3-(d), the 1x2 splitting performance is significantly improved with the metasplitter design, reducing the loss from 11.74 dB to 4.83 dB at 1580 nm, while also increasing the bandwidth. Similarly, Figure 3-(e) illustrates a more uniform 1x3 splitting operation across a broader wavelength range, with transmission ratios at 1580 nm—initially -13.71 dB, -3.73 dB, and -13.71 dB for the channels in the conventional strip waveguide configuration—improved to -6.48 dB, -6.09 dB, and -6.48 dB using the metasplitter design.

The measurement results for the 1DGW, 1x2, and 1x3 metasplitters are presented in Figure 3-(f) to (h), respectively. As shown in Figure 3-(f), the 1 dB bandwidth of the 1DGW is measured to be 38 nm, remaining nearly consistent with the simulation, with only a 1 nm reduction. Additionally, an average band shift of 26 nm is observed between the experimental and simulation results. Consequently, the simulated loss of 0.74 dB at 1580 nm corresponds to the loss measured at 1554 nm in the experiment, where the loss is recorded as 1.54 dB. For the 1x2 and 1x3 metasplitter structures, shown in Figure 3-(g) and (h), the minimum measured loss values are -5.05 dB and -6.51 dB, respectively, which align well with the simulation results of -4.80 dB for the 1x2 metasplitter and -6.09 dB for the 1x3 metasplitter. The additional loss introduced by fabrication imperfections is minor in all cases compared to the simulation results at 1580 nm, the point of minimal loss in the metasplitter designs. It is also important to note that the observed band shifts in both the 1DGW and the output ports of the metasplitters are attributed to the sensitivity of the 1DGW structure to dimensional variations [19], as well as the extremely small 100 nm feature size of the metastructures (Sect. S4, Supplement I).

As shown in the SEM images in Figure 3-(a) and (b), the effects of the 1DGW structure in terms of loss and bandwidth are also included in the transmission results provided in Figure 3-(d), (e), (g), and (h). However, to accurately assess the intrinsic performance of the metastructures, these 1DGW effects must be excluded from the transmission data. The resulting intrinsic transmission results for the metasplitters are presented

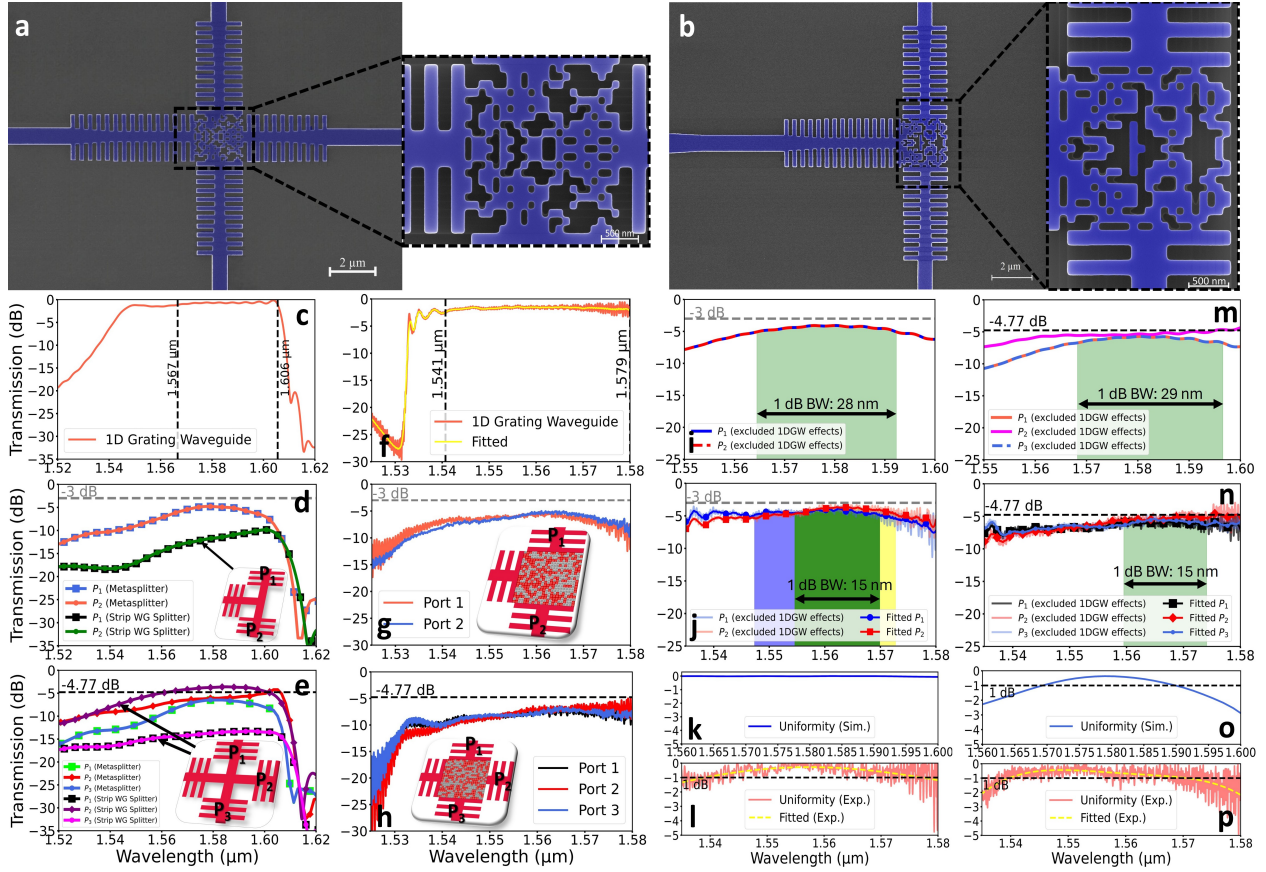


Figure 3: (a-b) SEM images of the 1x2 and 1x3 metasplitters. (c-e) Simulated transmission spectra for the 1DGW, strip waveguide, and metastructure-based splitters for 1x2 and 1x3 configurations. (f-h) Measured transmission spectra for the 1DGW, 1x2, and 1x3 metasplitters. (i-j) Simulated and measured intrinsic transmission results for the 1x2 metasplitter. (k-l) Simulated and measured uniformity for the 1x2 metasplitter. (m-n) Simulated and measured intrinsic transmission results for the 1x3 metasplitter. (o-p) Simulated and measured uniformity for the 1x3 metasplitter. In (o, p, l), the dashed line indicates the 1 dB level.

in Figure 3-(i) and (j) for the 1x2 configuration, and in Figure 3-(m) and (n) for the 1x3 configuration. In Figure 3-(i), the simulated loss for the 1x2 metasplitter at 1580 nm is 4.08 dB, with a 1 dB bandwidth of 28 nm. In Figure 3-(j), the measured results for the same structure show a minimum loss of 3.80 dB and a 1 dB bandwidth of 15 nm, where the 1 dB bandwidth limits of both channels intersect. Similarly, Figure 3-(m) presents, for the 1x3 metasplitter, an average simulated minimum loss of 5.61 dB at 1580 nm with a 1 dB bandwidth of 29 nm, while Figure 3-(n) shows the measured average minimum loss of 5.36 dB with a 15 nm 1 dB bandwidth, where the 1 dB bandwidth regions of all channels intersect. These results indicate losses of only 0.80 dB and 0.59 dB compared to ideal splitting operations (-3 dB for 1x2 (Figure 3-(j)) and -4.77 dB for 1x3 (Figure 3-(n))). Notably, the measured intrinsic transmission values of the metasplitters are slightly higher than the simulated results. This occurs because, when the 1DGW effects are excluded, band shift differences in the measured data cause slight alterations in transmission, leading to the observed increase in the measured transmission. To observe the difference between channels, the uniformity is calculated using the formula $U = -10 \cdot \log \left[\frac{\min(P_1 \times N)}{\max(P_1 \times N)} \right]$. As shown in Figure 3-(k) and (l) for the 1x2 metasplitter, the simulated uniformity is zero due to symmetrical conditions, while in the measurement results, it remains well

below 1 dB across a wide bandwidth. For the 1x3 metasplitter, as shown in Figure 3-(o) and (p), uniformity below 1 dB is consistently maintained across a wide bandwidth in both the simulation and measurement results.

In this Letter, we introduce the first Bloch mode metasplitter in 1x2 and 1x3 configurations for 1DGWs, designed to achieve the smallest possible footprint and low-loss wideband operation. The proposed study represents a novel structure for the photonic library and introduces genetic algorithm-based framework for increasingly prevalent time-domain-oriented inverse design approaches. While the proposed configurations are designed with the smallest possible footprint, the methodology is extendable to larger 1xN systems with diverse power distribution ratios. This study paves the way for advancements in complex optical antenna arrays and dense, high-bandwidth true-time-delay systems, fostering greater versatility and broader utilization of 1DGWs.

Acknowledgement

We would like to thank Prof. Lukas Chrostowski for his insightful comments and discussion. We also express our gratitude to the Silicon Electronic-Photonic Integrated Circuits (SiEPIC) program for their support.

Funding

This research was supported by the Scientific and Technological Research Council of Turkey (TUBITAK), project number 122E566. Ahmet O. Sakin acknowledges the support of the TUBITAK BIDEB 2210A grant.

Disclosures

The authors declare no conflicts of interest.

Data Availability Statement

Data underlying the results presented in this Letter are not publicly available but may be obtained from the authors upon reasonable request.

References

- [1] Maurizio Burla, Luis Romero Cortés, Ming Li, Xu Wang, Lukas Chrostowski, and José Azaña. Integrated waveguide bragg gratings for microwave photonics signal processing. *Optics express*, 21(21):25120–25147, 2013.
- [2] Weifeng Zhang and Jianping Yao. A fully reconfigurable waveguide bragg grating for programmable photonic signal processing. *Nature communications*, 9(1):1396, 2018.

- [3] Shengjie Xie, Yang Zhang, Yiwen Hu, Sylvain Veilleux, and Mario Dagenais. On-chip fabry-pérot bragg grating cavity enhanced four-wave mixing. *ACS Photonics*, 7(4):1009–1015, 2020.
- [4] Changhao Han, Zhao Zheng, Haowen Shu, Ming Jin, Jun Qin, Ruixuan Chen, Yuansheng Tao, Bitao Shen, Bowen Bai, Fenghe Yang, et al. Slow-light silicon modulator with 110-ghz bandwidth. *Science Advances*, 9(42):eadi5339, 2023.
- [5] Qiyuan Yi, Guanglian Cheng, Zhiwei Yan, Qiyuan Li, Fanglu Xu, Yongchao Zou, Ting Li, Yuhan Sun, Yi Zou, Yu Yu, et al. Silicon mmi-based power splitter for multi-band operation at the 1.55 and 2 μm wave bands. *Optics Letters*, 48(5):1335–1338, 2023.
- [6] Chaochao Ye and Daoxin Dai. Ultra-compact broadband 2×2 3 db power splitter using a subwavelength-grating-assisted asymmetric directional coupler. *Journal of Lightwave Technology*, 38(8):2370–2375, 2020.
- [7] Can Ozcan, Mo Mojahedi, and J Stewart Aitchison. Short, broadband, and polarization-insensitive adiabatic y-junction power splitters. *Optics Letters*, 48(18):4901–4904, 2023.
- [8] L He, HY Ji, YJ Wang, and XD Zhang. Topologically protected beam splitters and logic gates based on two-dimensional silicon photonic crystal slabs. *Optics Express*, 28(23):34015–34023, 2020.
- [9] Gencheng Wang, Tingge Dai, Jianfei Jiang, Xiaoqing Guo, Bei Chen, Yuehai Wang, Hui Yu, Xiaoqing Jiang, and Jianyi Yang. Continuously tunable true-time delay lines based on a one-dimensional grating waveguide for beam steering in phased array antennas. *Applied Optics*, 57(18):4998–5003, 2018.
- [10] Chi-Jui Chung, Xiaochuan Xu, Gencheng Wang, Zeyu Pan, and Ray T Chen. On-chip optical true time delay lines featuring one-dimensional fishbone photonic crystal waveguide. *Applied Physics Letters*, 112(7), 2018.
- [11] Byung-Min Jung, Jong-Dug Shin, and Boo-Gyoun Kim. Optical true time-delay for two-dimensional x -band phased array antennas. *IEEE photonics technology letters*, 19(12):877–879, 2007.
- [12] Xiangjie Zhao, Hamed Dalir, Xiaochuan Xu, and Ray T Chen. Efficient coupling into slow-light one-dimensional fishbone waveguide by mode converter method. *Applied Physics Express*, 10(7):072502, 2017.
- [13] Dries Vercruyse, Neil V Sapra, Ki Youl Yang, and Jelena Vuckovic. Inverse-designed photonic crystal circuits for optical beam steering. *ACS Photonics*, 8(10):3085–3093, 2021.
- [14] Cristian Della Giovampaola and Nader Engheta. Digital metamaterials. *Nature materials*, 13(12):1115–1121, 2014.
- [15] Amir Hosseini, Xiaochuan Xu, David N Kwong, Harish Subbaraman, Wei Jiang, and Ray T Chen. On the role of evanescent modes and group index tapering in slow light photonic crystal waveguide coupling efficiency. *Applied Physics Letters*, 98(3), 2011.

- [16] Daniel D Hickstein, David R Carlson, Haridas Mundoor, Jacob B Khurgin, Kartik Srinivasan, Daron Westly, Abijith Kowligy, Ivan I Smalyukh, Scott A Diddams, and Scott B Papp. Self-organized nonlinear gratings for ultrafast nanophotonics. *Nature Photonics*, 13(7):494–499, 2019.
- [17] Dries Verduynst, Neil V Saprà, Logan Su, and Jelena Vuckovic. Dispersion engineering with photonic inverse design. *IEEE Journal of Selected Topics in Quantum Electronics*, 26(2):1–6, 2019.
- [18] Lukas Chrostowski, Hossam Shoman, Mustafa Hammood, Han Yun, Jaspreet Jhoja, Enxiao Luan, Stephen Lin, Ajay Mistry, Donald Witt, Nicolas AF Jaeger, et al. Silicon photonic circuit design using rapid prototyping foundry process design kits. *IEEE Journal of Selected Topics in Quantum Electronics*, 25(5):1–26, 2019.
- [19] Hamed Saghaei, Payam Elyasi, and Bhavin J Shastri. Sinusoidal and rectangular bragg grating filters: design, fabrication, and comparative analysis. *Journal of Applied Physics*, 132(6), 2022.

Supplemental information:
**Ultra-miniaturized Bloch mode metasplitters for
one-dimensional grating waveguides**

Ahmet Oguz Sakin¹, Hamza Kurt², Mehmet Unlu^{1*}

¹Department of Electrical and Electronics Engineering, TOBB University of Economics and
Technology, Ankara, Turkey

²School of Electrical Engineering, Korea Advanced Institute of Science and Technology (KAIST),
Daejeon, Republic of Korea

***Corresponding author:** `munlu@etu.edu.tr`

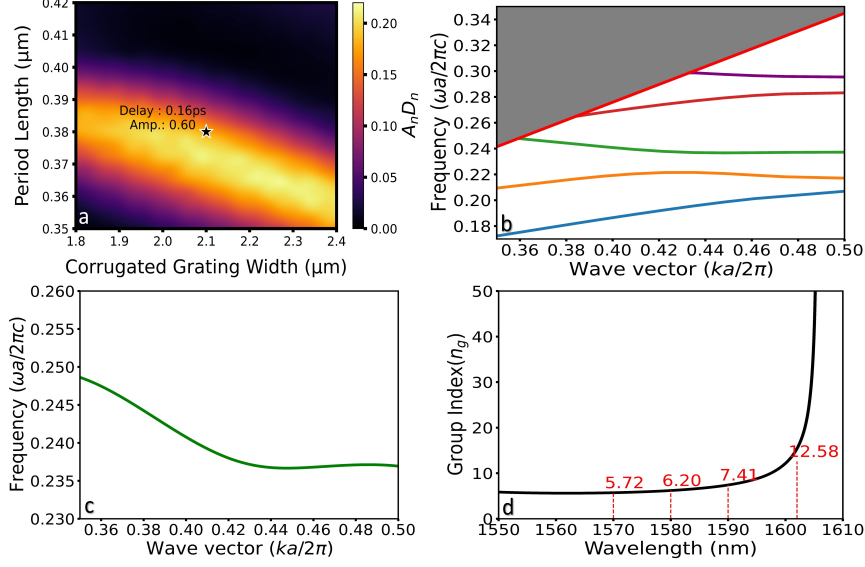
In this supplementary document, we begin with the design of one-dimensional grating waveguide (1DGW) topologies tailored for true time delay applications in the L-band. Following this, we derive analytical expressions that establish a correlation between the peak value of the time-domain Poynting vector, dispersion, and pulse broadening, facilitating the design of structures with optimal dispersion profiles and broadband characteristics. A thorough analysis of the electric field distribution across all structures is then provided. Lastly, we demonstrate the consistency between simulation and measurement results, tolerating the observed band shift between them.

S1 Design of one-dimensional grating waveguides for L-band applications

Figure S1 presents the key design criteria for the one-dimensional grating waveguide (1DGW) topology utilized in this study. The appropriate structural parameters of the 1DGW for L-band applications are determined by the product of the normalized peak power level, denoted as A_n , and the normalized true time delay, represented as D_n , for the 50-period structure. As illustrated in Figure S1-(a), the parameters are selected to facilitate the evaluation of metasplitter structures' performance in topologies near both optimized and non-optimized regions, based on time delay and peak power characteristics. Therefore, the corrugation width (w_d) is set to $2.1 \mu\text{m}$, and the grating period (λ) is set to 380 nm , with a 50% duty cycle. To generate this optimization, an ultrashort Gaussian signal with a width of 90 fs at 1580 nm is used as input to the system. The strip waveguide width (w_s) connecting the 1DGW to the grating coupler is chosen to support 2 TE and 2 TM modes, allowing for the evaluation of any potential mode conversion after the metasplitter devices. However, no such mode conversion was observed, owing to the superior mode protection provided by the meta devices. The inner waveguide width (w_c) is chosen as 450 nm to support an average level of dispersion, considering the width contrast with the strip waveguide width (w_s). The band diagram shown in Figure S1-(b) is calculated using the 3D plane wave expansion method, based on the optimized design parameters. As shown in Figure S1-(c), the relatively flat slope of band 3 corresponds to a low group velocity region. The group velocity, v_g , is expressed as $v_g = \frac{d\omega}{dk}$, where ω represents the angular frequency and k denotes the wave vector. In this region, the derivative $\frac{d\omega}{dk}$ is small, resulting in a low group velocity, a key characteristic of slow light. This slow light effect, coupled with the broad wavelength range over which it is sustained, makes band 3 highly suitable for true-time delay applications. The corresponding group index values are presented in Figure S1-(d). The group index n_g is determined to be 6.2 at 1580 nm , approximately 48% higher than that of a standard strip waveguide. This value increases to 12.58 at 1603 nm , clearly highlighting the significant design constraints associated with the wavelength-selective broadband nature of the metasplitter.

S2 Figure of merit formula for time-domain heuristic design with broadband and dispersion awareness

In the metasplitter design, the figure of merit of the time-domain heuristic algorithm is defined by the peak intensity of the time-domain Poynting vector at the output. This choice ensures that the design simultaneously



Supplementary Figure 1: (a) Design parameter space illustrating the relationship between the period length and the corrugated grating width, based on the product of normalized peak power and normalized time delay. (b) Band structure of the designed 1DGW. (c) Dispersion relation showing the frequency behavior of the selected mode. (d) Group index variation with respect to wavelength.

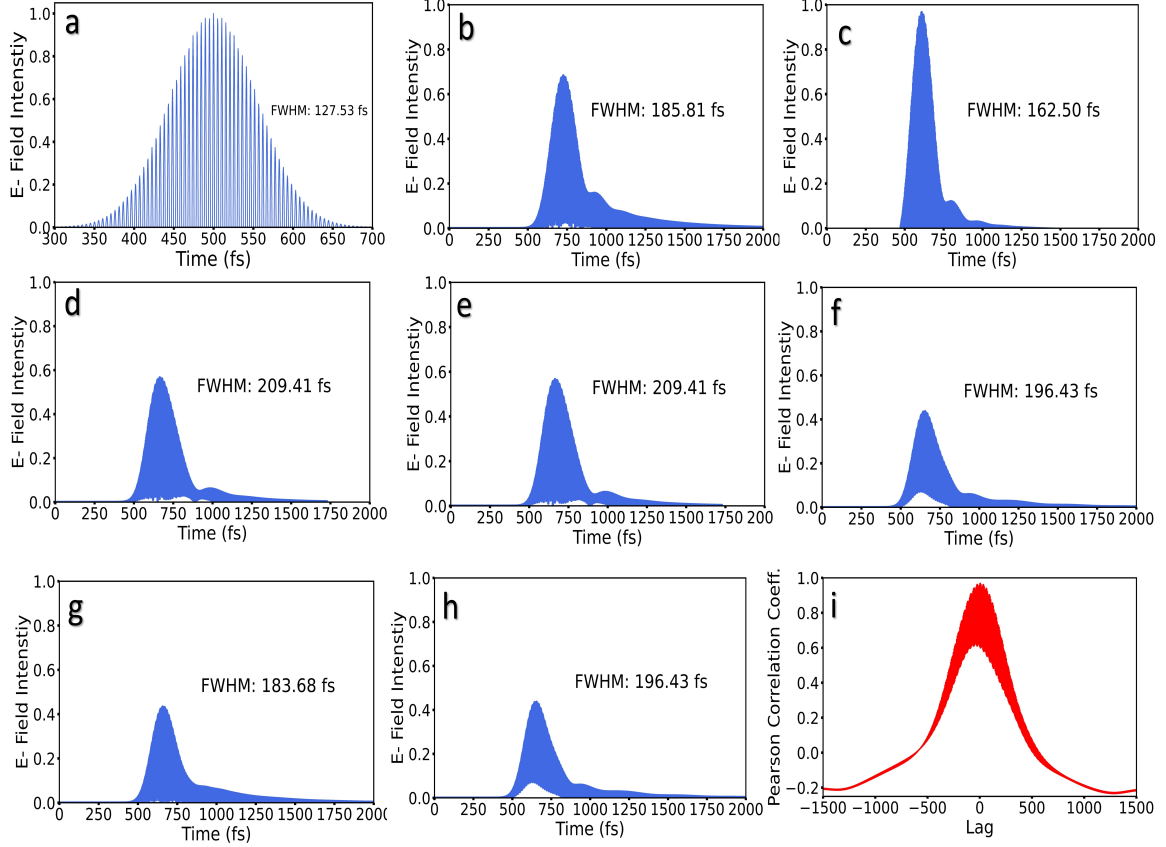
optimizes the wavelength-selective dispersion profile and broadband requirements without additional steps. Also, a Gaussian signal with a 90 fs pulse duration at 1580 nm is used to cover the targeted ultra-wideband range in the inverse design process. To demonstrate the appropriateness of the figure of merit, the Poynting vector output signal, after propagating through the dispersive medium of the 1DGW, is expressed in Equation S1.

$$S(t, z) = \frac{E_0^2}{\eta(z)} \exp\left(-\frac{t^2}{\tau(z)^2}\right) \cos^2(\omega_0 t + \phi(t, z)) \quad (\text{S1})$$

Here, $\tau(z)$ represents the broadened pulse duration at a distance z , ω_0 is the central angular frequency of the pulse, and $\phi(t, z)$ denotes the phase shift introduced by the dispersion. E_0 is the peak amplitude of the electric field, and $\eta(z) = \frac{\eta_0}{n(z)}$ represents the impedance of the medium, where η_0 is the intrinsic impedance of free space and $n(z)$ is the refractive index of the dispersive structure. The Gaussian pulse is typically symmetric in time, with the peak value of the time-domain Poynting vector occurring at the center of the pulse, at $t = 0$. As the pulse propagates through a dispersive medium, the pulse duration $\tau(z)$ increases due to broadening, which directly influences the peak value of the time-domain Poynting vector, $S_{\text{peak}}(z)$, since the energy is spread over a longer time frame. The derivation of the peak value of the time-domain Poynting vector is provided in Equation S2.

$$S_{\text{peak}}(z) \propto \frac{S_0}{\tau_0 \sqrt{1 + \left(\frac{z}{L_D}\right)^2}} \quad (\text{S2})$$

Here, τ_0 is the initial pulse duration, $L_D = \frac{\tau_0^2}{|\beta_2|}$ is the dispersion length, β_2 is the second-order dispersion coefficient, and S_0 is the peak value of the time-domain Poynting vector at $t = 0$. As demonstrated in Equation S2, the peak value of the time-domain Poynting vector is directly affected by both pulse broadening and the dispersion properties of the structure. Consequently, optimizing the peak value of the time-domain Poynting vector inherently involves achieving optimal dispersion and broadband characteristics.



Supplementary Figure 2: (a) Gaussian input signal. (b) Output from a 1DGW with 16 periods. (c) Corresponding output from half of the 16-period 1DGW structure. (d, e) Outputs for the 1x2 metasplitter structure. (f-h) Outputs for the 1x3 metasplitter structure: (f, h) symmetrical channels, (g) straight channel. (i) Pearson correlation coefficient calculation between symmetrical and straight channel outputs at different lag levels.

Due to the correlation between the E-field and the Poynting vector, as shown in Equation S1, the peak value of the time-domain Poynting vector is calculated using the E-field signal outputs. The corresponding E-field results are shown in Figure S2. Figure S2-(a) illustrates the Gaussian input signal employed in the heuristic optimization of the metastructures. Typically, each channel in the metasplitter structures consists of 16 periods of the 1DGW from input to output. Figure S2-(b) shows the output of the ultrashort pulse signal from a 1DGW with 16 periods, where the peak E-field intensity is approximately 0.63, resulting in a peak power intensity of about 0.4, as the peak power intensity is proportional to the square of the peak E-field intensity. The power monitors in the 3D Finite-Difference Time-Domain (FDTD) simulations, used to characterize the time-domain response of metasplitter designs, are placed at the tip of the meta structures, covering only

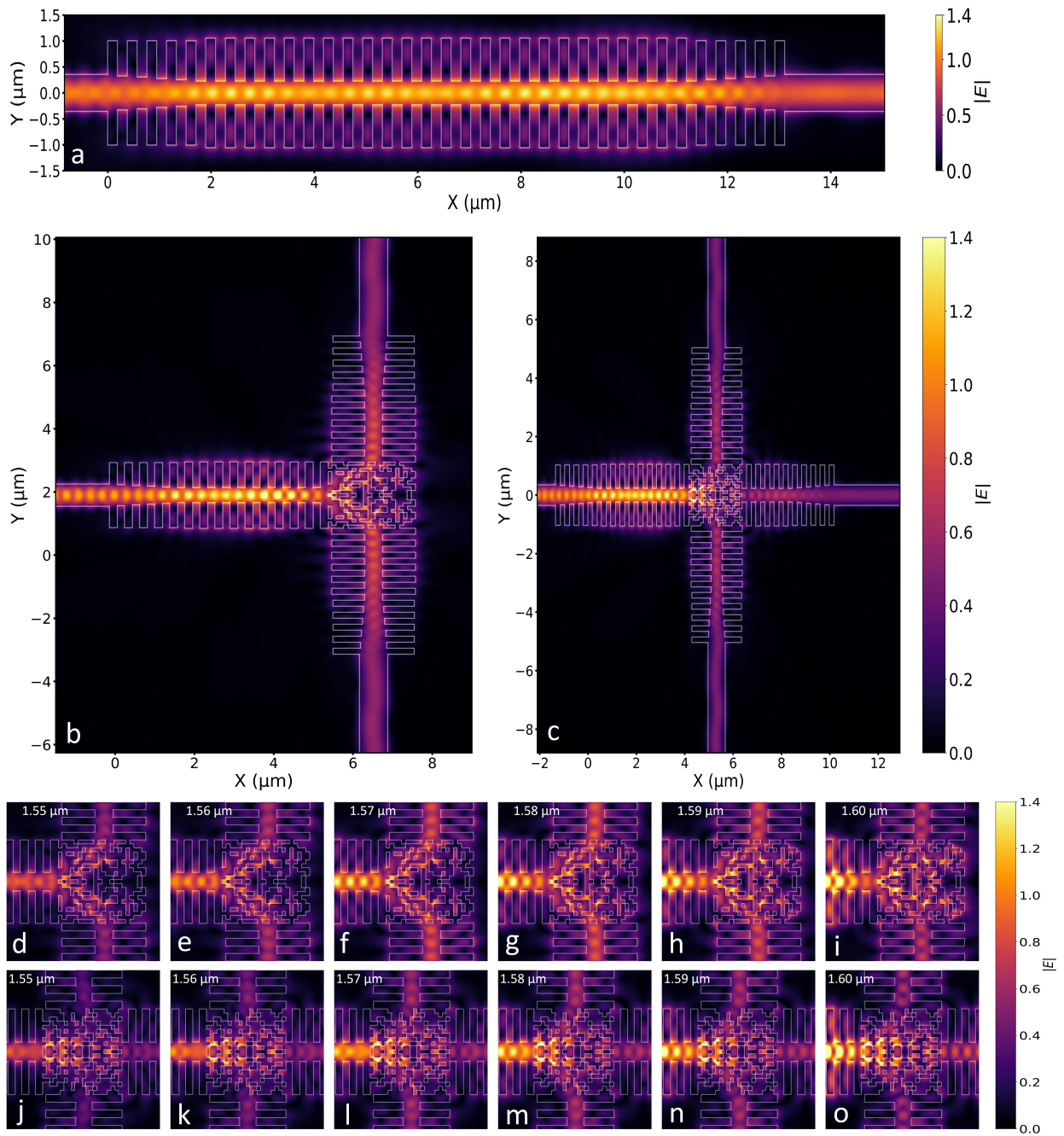
half of the 16-period 1DGW. Therefore, the analysis should also include the half-system of the 16-period 1DGW, as illustrated in Figure S2-(c). In this configuration, the peak E-field intensity reaches approximately 0.98, corresponding to the peak power intensity of 0.96. Figure S2-(d) and (e) depict the outputs for the 1x2 metasplitter structure, which shows symmetry in both channels, resulting in identical outputs. The peak E-field intensity is approximately 0.57, resulting in the peak power intensity of 0.65 across the two channels, with a Full Width at Half Maximum (FWHM) expansion of 47 fs compared to the half-system of the 1DGW. Figure S2-(f) to (h) illustrate the outputs for the 1x3 metasplitter structure: (f) and (h) show the symmetrical channels, while (g) displays the straight channel. The average peak power intensity is 0.56, with FWHM expansions of 33 fs for the symmetrical ports and 20 fs for the straight channel. Moreover, to assess the similarity between the symmetrical and straight channel outputs, the Pearson correlation coefficient is calculated. As shown in Figure S2-(i), a value very close to 1 is obtained at lag 0, indicating a high degree of similarity. As a result of the examined scenarios, it is evident that the deviation ratio remains notably low despite using an ultra-miniature structure. This preservation of peak intensity enables the design of a meta-structure with low loss, uniform characteristics, and broadband frequency response, as stated in the main text.

S3 Electric field mode distributions

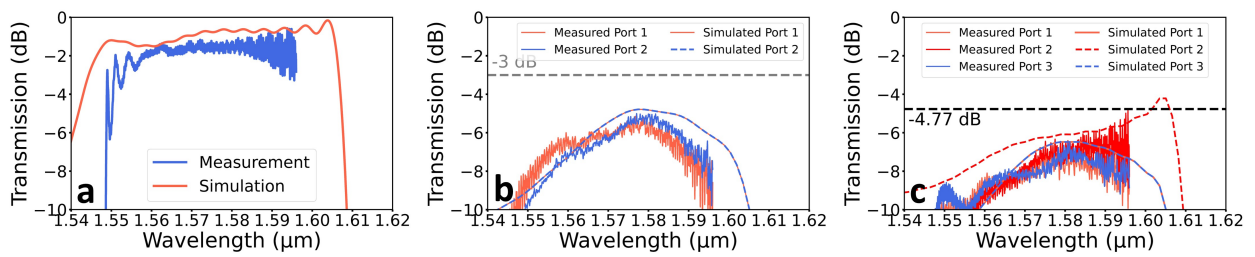
Figure S3-(a) to (o) presents the E-field mode distributions for both the 1DGW and the designed metastructures. Figure S3-(a) to (c) shows the results at 1580 nm. For the 1x2 splitter, Figure S3-(d) to (i) illustrates the field distributions, and for the 1x3 metasplitters, Figure S3-(j) to (o) details the distributions within the 1550-1600 nm range for both structures.

S4 Analysis of band shift between simulations and measurements

As outlined in the main text, the 1DGW structure exhibits significant sensitivity to dimensional variations, such as sidewall roughness, period, and corrugation width. Fabrication imperfections cause shifts in the band structure due to alterations in these parameters. Additionally, the small pixel size of 100 nm introduces fabrication imperfections, such as rounded corners in metastructures, which further affect the uniformity ratio between channels in metasplitter designs. When comparing the 1 dB bandwidths of the measurement and simulation results presented in the main text, the average shift is found to be 26 nm for the 1DGW, 13 nm for the 1x2 metasplitter, and 9 nm for the 1x3 metasplitter, resulting in an overall average shift of 16 nm. The band narrowing is disregarded due to its minimal impact, as it is calculated to be only 1 nm between the simulated and measured results for the 1DGW structure. As shown in Figure 4S-(a) to (c), when the measurement results are shifted by 16 nm, the 1DGW, 1x2, and 1x3 metasplitters respectively demonstrate that the measurement and simulation results are in good agreement.



Supplementary Figure 3: (a-c) E-field mode distributions for the 1DGW and designed 1x2 and 1x3 metastructures at 1580 nm, respectively. (d-i) E-field distributions for the 1x2 metasplitter across the 1550-1600 nm range. (j-o) E-field distributions for the 1x3 metasplitter within the same wavelength range.



Supplementary Figure 4: Comparison of measured and simulated transmission after applying a 16 nm shift to the measured data. (a) for the 1DGW, (b) for the 1x2 metasplitter, and (c) for the 1x3 metasplitter.